Journal of Materials Science & Technology 119 (2022) 190–199

Contents lists available at ScienceDirect

Journal of Materials Science & Technology

journal homepage: www.elsevier.com/locate/jmst

Research Article

High entropy ultra-high temperature ceramic thermal insulator $(Zr_{1/5}Hf_{1/5}Nb_{1/5}Ta_{1/5}Ti_{1/5})C$ with controlled microstructure and outstanding properties

Zhuojie Shao[a,b], Zhen Wu[a,*], Luchao Sun[a], Xianpeng Liang[a,b], Zhaoping Luo[a], Haikun Chen[c], Junning Li[c], Jingyang Wang[a,*]

[a] Shenyang National Laboratory for Materials Science, Institute of Metal Research, Chinese Academy of Sciences, Shenyang 110016, China
[b] School of Materials Science and Engineering, University of Science and Technology of China, Hefei 230026, China
[c] Science and Technology on Advanced Functional Composites Laboratory, Aerospace Research Institute of Materials and Processing Technology, Beijing 100076, China

ARTICLE INFO

Article history:
Received 9 October 2021
Revised 30 November 2021
Accepted 3 December 2021
Available online 2 March 2022

Keywords:
High entropy UHTCs
High porosity
High strength
Low thermal conductivity
Oxidation resistance

ABSTRACT

Due to advancements of hypersonic vehicles, ultra-high temperature thermal insulation materials are urgently requested to shield harsh environment with superhigh heat flux. Toward this target, ultra-high temperature ceramics (UHTCs) are the only choice due to their excellent capability at ultra-high temperatures. We herein report a novel highly porous high entropy $(Zr_{1/5}Hf_{1/5}Nb_{1/5}Ta_{1/5}Ti_{1/5})C$ fabricated by foam-gelcasting-freeze drying technology combined with in-situ pressureless reaction sintering. The porous $(Zr_{1/5}Hf_{1/5}Nb_{1/5}Ta_{1/5}Ti_{1/5})C$ exhibited ultra-high porosity of 86.4%-95.9%, as well as high strength and low thermal conductivity of 0.70–11.77 MPa and 0.164–0.239 W/(m·K), respectively. Specifically, SiC sintering additive only locates at the pit of the surface of sintering neck between UHTC grains, and there is no secondary phase or intergranular film at the grain boundary. Besides, the oxidation resistance of high entropy carbide powders is greatly improved compared with that of the mixed five carbide powders. This work clearly highlights the merits of highly porous high entropy $(Zr_{1/5}Hf_{1/5}Nb_{1/5}Ta_{1/5}Ti_{1/5})C$ as an ultra-high temperature thermal insulation material.

1. Introduction

Due to advancement of hypersonic vehicles and critical requests for a faster speed, aerodynamic heating protection becomes more serious [1], which results in the service temperature of thermal insulation component above 2000 °C. However, common oxide thermal insulation materials cannot survive under such ultra-high temperature environment due to their relatively low melting points [2–5]. Hence, it is urgent to develop new ultra-high temperature insulation materials that demonstrate high strength, outstanding thermal stability and extremely low thermal conductivity.

Transition metal carbides, nitrides, and borides belong to the well-known class of ultra-high temperature ceramics because of their very high melting points [6]. Among them, ultra-high temperature carbides ZrC, HfC, NbC, TaC and TiC are promising ultra-high temperature thermal insulation materials, which stem from their high melting temperature (>3000 °C), excellent thermochemical stability, high strength and ablation resistance [7,8]. However, the intrinsic thermal conductivity of these ultra-high temperature carbides is considerably high, for instance, 33.5 W/(m·K) for ZrC and 29.3 W/(m·K) for HfC [9]. Therefore, it is challenged to make effective modifications to reduce thermal conductivity, so that they can satisfy the requirements for thermal insulation materials. Generally, enhancing the porosity and high entropy effect are two methods to decrease thermal conductivity. It is well known that realizing ultra-high porosity (>90%) could obtain extremely low thermal conductivity [10]. In addition, the significant lattice inhomogeneity arising from high entropy adoption may inhibit heat transportation through the lattice, and subsequently reduces thermal conductivity of a high entropy ceramic [11]. A good example is demonstrated by the very low thermal conductivity of high entropy carbide $(Zr_{0.2}Hf_{0.2}Ti_{0.2}Nb_{0.2}Ta_{0.2})C$ that has a value of 6.45 W/(m·K) [9]. The magnitude is much lower than the averaged thermal conductivity (24.96 W/(m·K)) of the five binary carbides. A proper combination of the above two methods can lead to a lower thermal conductivity of ultra-high temperature carbide. To date, high en-

* Corresponding authors.
E-mail addresses: zwu@imr.ac.cn (Z. Wu), jywang@imr.ac.cn (J. Wang).

https://doi.org/10.1016/j.jmst.2021.12.030
1005-0302/

tropy carbide ($Zr_{0.2}Hf_{0.2}Ti_{0.2}Nb_{0.2}Ta_{0.2}$)C with 80.99% porosity was successfully fabricated and displayed moderately high compressive strength of 3.45 MPa and low room-temperature thermal conductivity of 0.39 W/(m·K) [12], which supports the feasibility of aforementioned perspective. Besides, it is still a challenge for both ultra-high porosity (~95%) and high strength. Predictably, if high porosity and high strength are simultaneously realized, the high entropy ultra-high temperature ceramics with light weight and excellent heat-shielding performance would be obtained.

In general, the sintering of highly porous UHTCs is very difficult because of their superhigh melting point and low self-diffusion coefficient [13]. Previous works on processing dense UHTC samples demonstrated that it was hard to obtain highly compact material even by using Spark Plasma Sintering (SPS) or Hot-Pressing (HP) method above 2000 °C. It was reported that TaC sample only reached the density of 92% by using SPS technique under pressure of 30 MPa at 2300 °C [14]. As for high entropy UHTCs, the sintering and multi-component solid solution of principal elements are harder than those of a sample with single principal element. Consequently, nearly all reported works were subjected to reactive sintering by SPS and HP at relatively high temperatures of 2200–2300 °C [9,15-18]. Evidently, it is necessary to adopt external driving force to densify UHTCs. In this context, multifarious sintering additives such as SiC, WC, $MoSi_2$, $TaSi_2$, B_4C and C were employed to promote sintering kinetics of UHTCs, which facilitated the removal of surface oxides [19–22]. Among these additives, SiC has attracted great interest, because it not only enhanced sinterability, but also improved mechanical properties and oxidation resistance of ultra-high temperature ceramics [22]. Until now, SiC was basically added as a composite component in many literatures about high entropy ceramics. Thereinto, SiC was found to play an essential role in phase formation during sintering of high entropy UHTCs (borides or carbides)/SiC composites [23]. Besides, SiC-reinforced high entropy carbides have been reported to show remarkable mechanical properties by Lu et al. [24] and oxidation resistance by Wang et al. [25]. Although SiC presents as a good sintering additive, it may be deleterious to high-temperature mechanical properties due to residual secondary phases or amorphous intergranular film between matrix grains [26–28]. Thus, what counts is dedicated to clean grain boundary phase to avoid affecting high temperature performance.

In this work, our ambition was to develop ultra-high porosity high entropy carbide thermal insulator with lighter weight, higher strength, lower thermal conductivity, and better oxidation resistance by pressureless sintering at relatively low temperature. Herein, foam-gelcasting-freeze drying technology, multi-component high entropy effect, and SiC sintering additive were used to realize the above targets. Phase composition, microstructure and compositional homogeneity of as-prepared samples were comprehensively characterized. Compressive strength and thermal conductivity, as well as the oxidation behavior of high entropy carbide powders were investigated. Specifically, clean grain boundary in porous high entropy carbide ($Zr_{1/5}Hf_{1/5}Nb_{1/5}Ta_{1/5}Ti_{1/5}$)C skeleton was observed and discussed.

2. Experimental

2.1. Starting materials and preparation procedure

Commercially available ZrC (≥99%, ~1 μm), HfC (≥99%, ~0.8 μm), NbC (≥99%, ~1–3 μm), TaC (≥99.6%, ~1–3 μm) and TiC (≥99.5%, ~1–2 μm) (Forsman Scientific (Beijing) Co., Ltd.) were used as raw materials for synthesizing ultra-high porosity high entropy UHTC in this study. The five transition metal carbides with equal molar ratio were mixed by using Si_3N_4 jars with Si_3N_4 balls and absolute ethyl alcohol as media. The mixture was milled at 300 rpm for 24 h by using a planetary ball mill. After ball-milling, the slurry was dried in an oven at 80 °C and then sieved through a 200-mesh screen. The SiC (≥99%, ~500 nm, Shanghai Chao Wei Nanotechnology Co., Ltd.) was used as sintering additive. Different SiC additions (0 wt.%, 0.3 wt.%, 0.6 wt.%, 1.0 wt.% and 2.0 wt.%) were added to promote sintering of UHTC powders. Long-chain surfactant sodium dodecyl sulfate (SDS) was used as foaming agent. A typical procedure of preparing ultra-high porosity high entropy UHTCs was as follows [29]. Firstly, the mixed powders, SiC powder and ammonium citrate were added into deionized water and stirred well. Then SDS was added into the above suspension under vigorous stirring to foam and then the foamed suspension was heated. Next the gelatin was added, and agitation remained for 10 min. Afterward, the foams were poured into a mold, then frozen and dried in a vacuum freeze dryer (SCIENTZ-10N, Scientz, Ningbo, China). After demoulding, the green bodies were pre-sintered at 1500 °C for 2 h. Finally, the pre-sintered samples were heated at 2000 °C for 2 h by using a vacuum graphite tube furnace (MT-18–22, Chen Hua, Shanghai, China). The porous high entropy carbide samples prepared from different solid contents of 7, 10, 15 and 20 vol.% as well as 2 wt.% SiC aiddtive were designated as HEC-7, HEC-10, HEC-15 and HEC-20, respectively. Where HEC represents pure-phase porous high entropy carbide with 2 wt.% SiC additive in this work.

2.2. Characterization

Phase composition was characterized via a step-scanning X-ray diffraction (XRD) (Rigaku D/max-2400, Tokyo, Japan) with Cu K_α radiation (λ=1.54178 Å) over a 2θ range of 20°−80° by using 0.02° steps. Porosity (P) was calculated by Eq. (1):

$$P = \left(1 - \frac{\rho}{\rho_t}\right) \times 100\% \quad (1)$$

where ρ is the apparent density of porous high entropy carbide, which is computed by ratio of measured mass to volume; ρ_t is theoretical density of dense bulk high entropy carbide ($Zr_{1/5}Hf_{1/5}Nb_{1/5}Ta_{1/5}Ti_{1/5}$)C, which is computed by its lattice parameter, and where the lattice parameter is calculated from XRD data. X-ray tomography analysis (XRT) (Xradia Versa XRM-500, Xradia, Pleasanton, USA) was applied to compute porosity of porous high entropy carbide by an Arizo fire software, which can present tridimensional microstructure of the sample. Scanning electron microscope (SEM) (SUPRA 55, Zeiss, Oberkochen, Germany) equipped with an electron dispersive spectroscopy (EDS) and transmission electron microscope (TEM) (Titan Cubed Themis G3 300, FEI, Oregon, USA) with EDS were used to analyze the microstructure and compositional uniformity. Compressive strength was tested by a universal testing machine (CMT 4204, SANS, Shenzhen, China) at a loading speed of 0.5 mm/min. Five samples with a dimension of about Φ20 mm × 20 mm were used to determine compressive strength. Thermal conductivity was measured from room temperature to 300 °C by guarded heat flow test method (DTC-300, TA Instruments Co., New Castle, USA) with a sample size of Φ50.5 mm × 2.5 mm. The oxidation behaviors of high entropy carbide powders and mixed raw powders were compared by using a thermogravimetric analysis combined with differential scanning calorimetry (TG-DSC) (STA449F3, Netzsch, Selb, Germany) from room temperature to 1400 °C under airflow at a heating rate of 5 °C/min.

3. Results and discussion

3.1. Phase compositions

XRD patterns of the as-prepared samples with different SiC additive contents together with the mixed powders are shown in

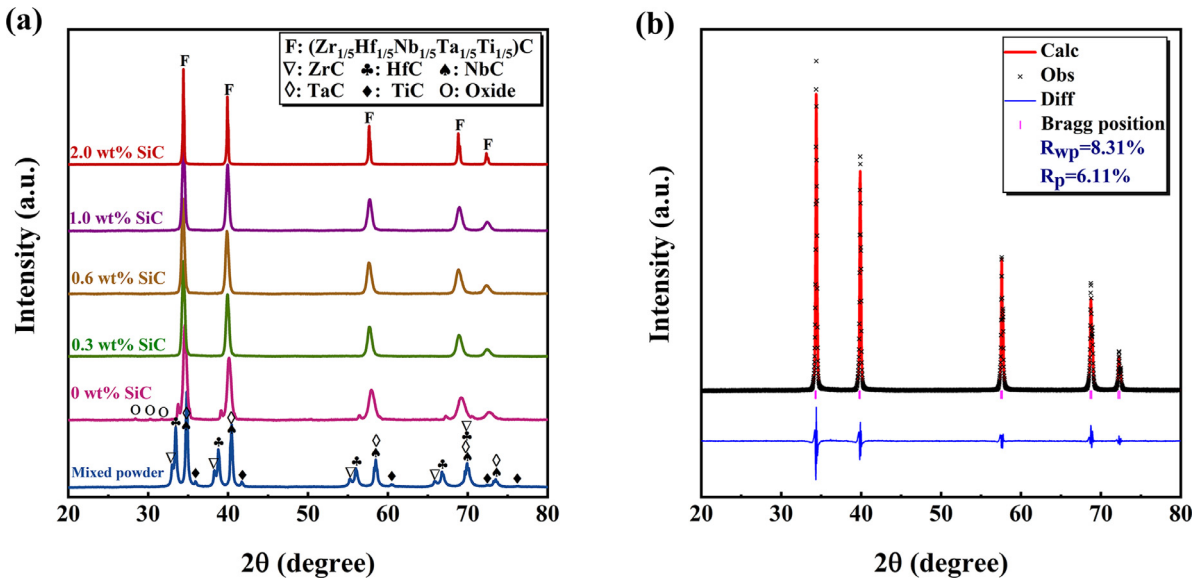

Fig. 1. (a) XRD patterns of mixed powders and sintered samples with different SiC contents; (b) Rietveld refinement pattern of sample with 2 wt.% SiC content.

Fig. 1(a). Diffraction peaks of the mixed powders correspond to five binary carbides respectively, which indicates that after ball milling, the mixed powders are just the mixture of ZrC, HfC, NbC, TaC and TiC. Based upon Fig. 1(a), the sample without SiC additive obviously does not complete the solid solution process, and diffraction peaks of oxides are detected. The formation of oxides may be primarily derived from the oxidation by some oxygen-containing substances generated from the pyrolysis of organics added during preparation process of porous green body. For the sample without SiC additive, the completion of solid solution and removal of residual oxides both need a prolonged annealing time or a higher heating temperature. In particular, a single-phase of rock-salt structure without oxide peaks is formed with addition of SiC and does not show any preferred orientation. Moreover, the width of XRD diffraction peaks gets narrower with the increase of SiC content, which indicates improved crystallinity. It is suggested that SiC not only serves as sintering additive to lower the solid solution temperature, but also acts as a reducing agent to consume the residual oxygen during the preparation of sample. As shown in XRD patterns, 2 wt.% SiC content shows the best crystallinity, and thus this content is used as optimal addition amount in this work.

Rietveld refinement was carried out to gain information about the lattice parameters by using General Structural Analysis System (GSAS) program, as shown in Fig. 1(b). It yields good refinement statistics of R_p=8.31% and R_{wp}=6.11%. Calculated lattice parameter of sample with 2 wt.% SiC is 4.530 Å, which is larger than the values of 4.5084 Å [30], 4.5180 Å [9] and 4.5244 Å [15] reported in previous works. It was reported that solid solution of oxygen (lattice oxygen) in carbide lattice will result in decrement of lattice parameter due to smaller atomic radius of oxygen in comparison with carbon atom [31,32]. The higher lattice parameter in this work provides a hint of low oxygen content. On the basis of lattice parameter, theoretical density (ρ_t) is calculated to be 9.37 g/cm^3. Then the porosity of porous sample is calculated according to this value.

3.2. Microstructure of porous high entropy carbide

Fig. 2 presents micrographs of HEC-10, HEC-15 and HEC-20. It reveals that all samples exhibit a uniform isotropic multiple pore structure, including large pores, windows and small pores in the skeleton. As displayed in Fig. 2(a), (d) and (g), size distributions of large pores for HEC-10, HEC-15 and HEC-20 are about 65–296 μm, 67–267 μm and 60–242 μm, respectively. Thereinto, some of larger pores might be related to the merging of two or more pores. Size distributions of the windows for HEC-10, HEC-15 and HEC-20 are about 19–155 μm, 13–130 μm and 12–110 μm, respectively. Small pores in the cell wall are observed in Fig. 2(b), (e) and (h), and their size distributions are around 0.2–4.7 μm, 0.2–4.2 μm and 0.2–3.5 μm, respectively. As can be seen, there are only very few small pores in the cell wall which is nearly dense skeleton, which contributes to good mechanical properties. Fig. 2(c), (f) and (i) display the well-sintering of neighboring particles and grain growth of high entropy UTHC grains. The particle sizes are 0.35–4.91 μm, 0.22–3.63 μm and 0.11–2.40 μm, and the mean values are about 2.17 μm, 1.31 μm and 0.85 μm for HEC-10, HEC-15 and HEC-20, respectively.

Fabricated samples with different solid contents all have uniformly interconnected pores and thin cell wall, resulting in their ultra-high porosity. As solid content increases, there is a little decrease in the sizes of large pores, windows and small pores. The number of small pores is significantly reduced, while a modest lift of skeleton thickness appears. This is because that the viscosity of slurry increases with the increase of solid content; and a higher viscosity in a certain range and higher solid content tend to bring out smaller pores, narrower pore distribution, thicker cell walls, and better integrity of pores. In terms of particle size, size distribution is narrower and mean particle size is smaller with solid content increasing. In the case of low solid content, there are larger surface area, thinner cell wall and shorter pore channel in samples causing faster volatilization for SiC additive. Hence, there is longer time for grain growth in the sample with lower solid content, so its grain is larger than those with higher solid contents. Additionally, all samples exhibit nearly dense skeleton, which benefits from the improvement of sinterability by adding SiC additive. Properties of porous ceramic are significantly affected by their microstructure. The firmly sintered skeleton and strong cell wall are of great importance to achieve good mechanical property [33].

X-ray tomography measurement was employed to reconstruct three-dimensional morphology of HEC-20. As shown in Fig. 3(a), a large field of view with a low resolution of 3.1 μm (small pores in the wall are indistinguishable in the figure) is used to characterize large pores and cell windows. As can be seen, it presents uniform interlinking pores in the sample, and it clearly shows that

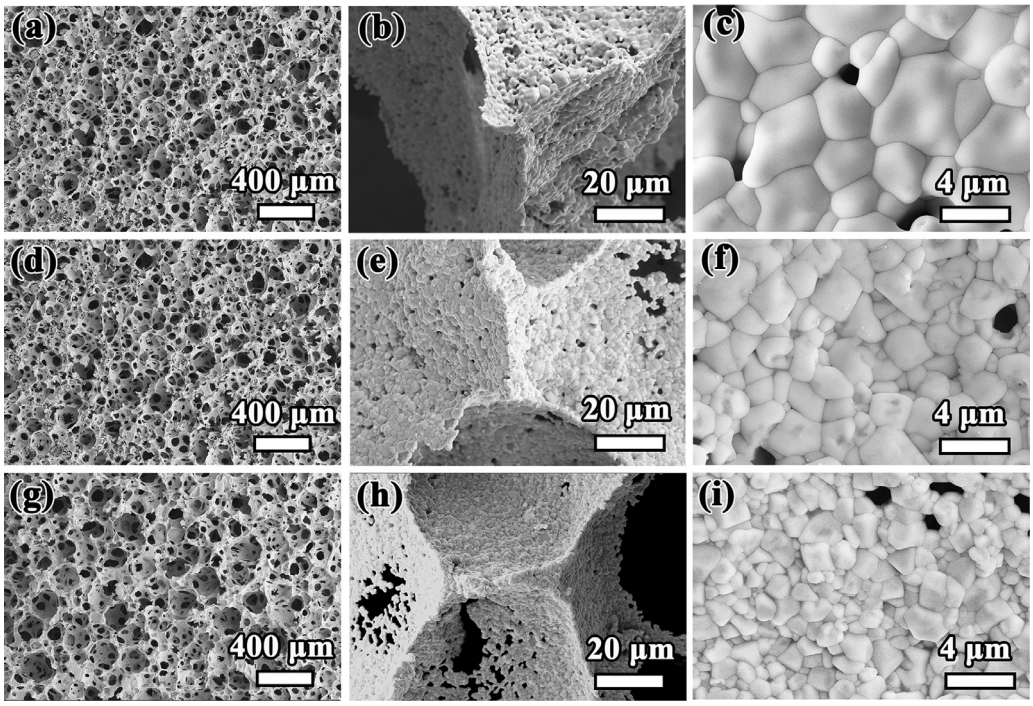

Fig. 2. SEM images of large pores, cell wall and crystal grains for porous high entropy carbide samples: (a)-(c) for HEC-10, (d)-(f) for HEC-15 and (g)-(i) for HEC-20.

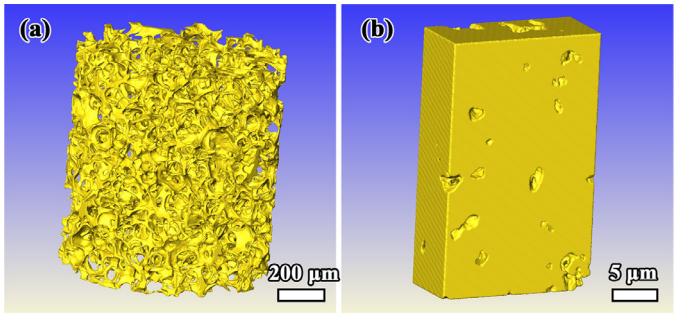

Fig. 3. XRT images of porous high entropy carbide: (a) large pores and (b) cell wall for HEC-20.

the sizes of large pores are generally below 250 μm. Besides, in order to analyze small pores in the cell wall, a microscopic field of view with a resolution of 64 nm is shown in Fig. 3(b). There are a few small pores (0.3–3.1 μm) in the skeleton, and it indicates a relatively dense skeleton. XRT results accord closely with the results provided by SEM image analysis. In the light of reconstructed spatial distribution, the volume fraction of large pores and small pores are computed, which are 86.5% and 7.9%, respectively. Total volume fraction of pores is 87.6% and it is close to the value of 86.4% that was calculated by Eq. (1).

3.3. Compositional homogeneity of porous high entropy carbide

To manifest the compositional homogeneity of porous high entropy carbide, EDS mappings of SEM and TEM at different scales were characterized. SEM image at a microscale and corresponding EDS mappings of Zr, Hf, Nb, Ta and Ti are displayed in Fig. 4. It shows that the highly uniform distributions of the five transition metal elements without segregation. It suggests that the solid solution process of five principal elements is complete and the solution is homogeneous on microscale. Furthermore, the average atomic percentages are almost equal, which agrees with expected equiatomic composition of $(Zr_{1/5}Hf_{1/5}Nb_{1/5}Ta_{1/5}Ti_{1/5})C$.

Fig. 5 shows the microstructure, selected area electron diffraction (SAED) pattern, and corresponding EDS mappings at nanoscale. High-angle Annular Dark Field (HAADF) image and corresponding Annular Bright Field (ABF) image present a periodic symmetric atomic lattice, as shown in Fig. 5(a) and (b), in which a set fringe is about 2.267 Å, corresponding to d-space of (200) plane of face centered cubic (FCC) high entropy carbide. The lattice parameter calculated from the interplanar spacing is about 4.534 Å, which is close to the value of 4.530 Å obtained by XRD Rietveld refinement. SAED pattern along [001] zone axis shown in Fig. 5(c) indicates that the as-prepared sample has a typical FCC structure, which is in good agreement with XRD results. All intensity maps of Fig. 5(d)-(i) clearly demonstrate the compositional and structural homogeneity at atomic scale. Both results based on different magnifications reveal that the porous sample consists of a chemically and structurally homogeneous high entropy material.

Combined with the forementioned characterization methods of XRD, XRT, SEM and TEM, we conclude that the porous single-phase high entropy carbide $(Zr_{1/5}Hf_{1/5}Nb_{1/5}Ta_{1/5}Ti_{1/5})C$ with good compositional uniformity at both microscale and atomic scale is successfully synthesized by foam-gelcasting-freeze drying method and in-situ pressureless reaction sintering.

3.4. Compressive strength and thermal conductivity

Compressive strength is one of the most important mechanical properties for porous ceramics. While thermal conductivity is a crucial index to measure thermal insulation materials. As is well-known, porosity has a great influence on strength and thermal conductivity. Fig. 6 displays the dependance of compressive strength and thermal conductivity on porosity for our samples. In Fig. 6(a), it is seen that compressive strength of porous high entropy carbide decreases from 11.77 to 0.70 MPa with porosity varying from 86.4% to 95.9%. The pore morphology, pore size distribution, strut thickness and densification of cell wall all have notice-

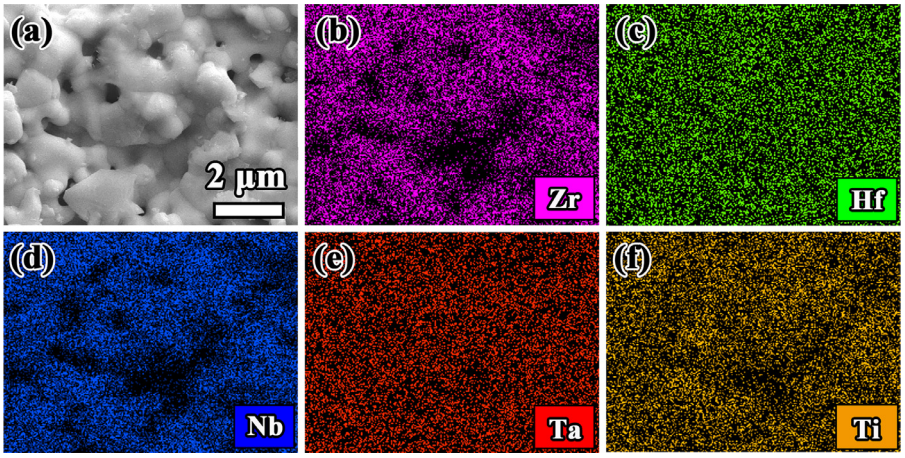

Fig. 4. SEM-EDS analysis of $(Zr_{1/5}Hf_{1/5}Nb_{1/5}Ta_{1/5}Ti_{1/5})C$: (a) SEM image, and (b)-(f) corresponding EDS mappings.

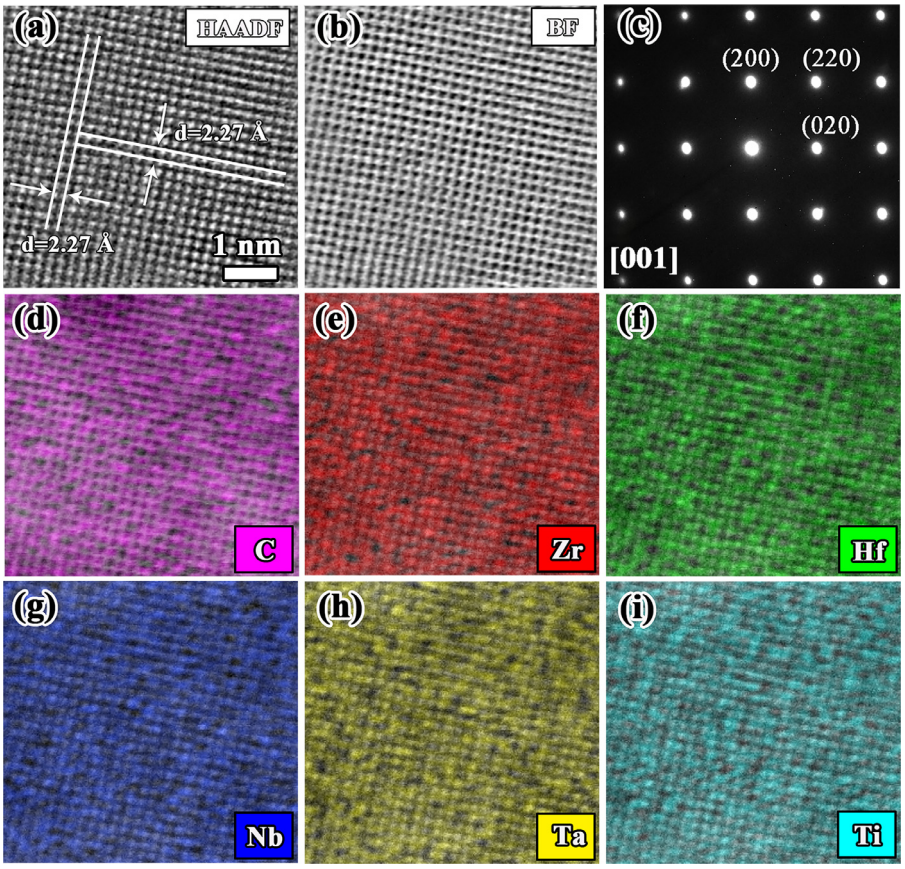

Fig. 5. STEM-EDS analysis of porous high entropy carbide sample: (a) HAADF image, (b) corresponding ABF image, (c) SAED pattern and (d)-(i) corresponding EDS mappings.

able effects on the strength of porous materials. As porosity increases, it is obviously presented in Fig. 2 that pore size distribution gets larger and the cell wall becomes thinner, which results in relatively weak ability to resist external load and yields lower strength. Vice versa, the porous sample with lower porosity has higher strength due to smaller pore size and thicker cell wall. It should be mentioned here that the strength of our samples is superior to those of other porous oxides and carbides with similar porosities [34–39], which are plotted and compared in Fig. 6(a). It is noted that the strength (11.77 MPa, porosity: 86.4%) in this work is higher than that (3.45 MPa, porosity: 80.99%) of porous $(Zr_{0.2}Hf_{0.2}Ti_{0.2}Nb_{0.2}Ta_{0.2})C$ [12]. The basic reason is due to differences in microstructure. Concretely, owing to high sintering temperature and the use of SiC sintering additive, our sample has tighter sintering neck, denser skeleton and larger contact area of grain than those obtained from partial sintering method. Besides, when compared with the work of highly porous multicomponent $(Hf_{1/3}Ta_{1/3}Nb_{1/3})C$ of our team [40], the higher strength in this work is also due to differences in micromorphology. To be specific, the addition of SiC dramatically accelerates the sintering of UHTCs powders and generates dense and firm skeleton in this study, rather than the porous skeleton of porous $(Hf_{1/3}Ta_{1/3}Nb_{1/3})C$ without using any sintering aids [40].

Fig. 6(a) also shows that room temperature thermal conductivity of porous samples in this study varies from 0.239 to 0.164 W/(m·K) as porosity increases from 86.4% to 95.9%.

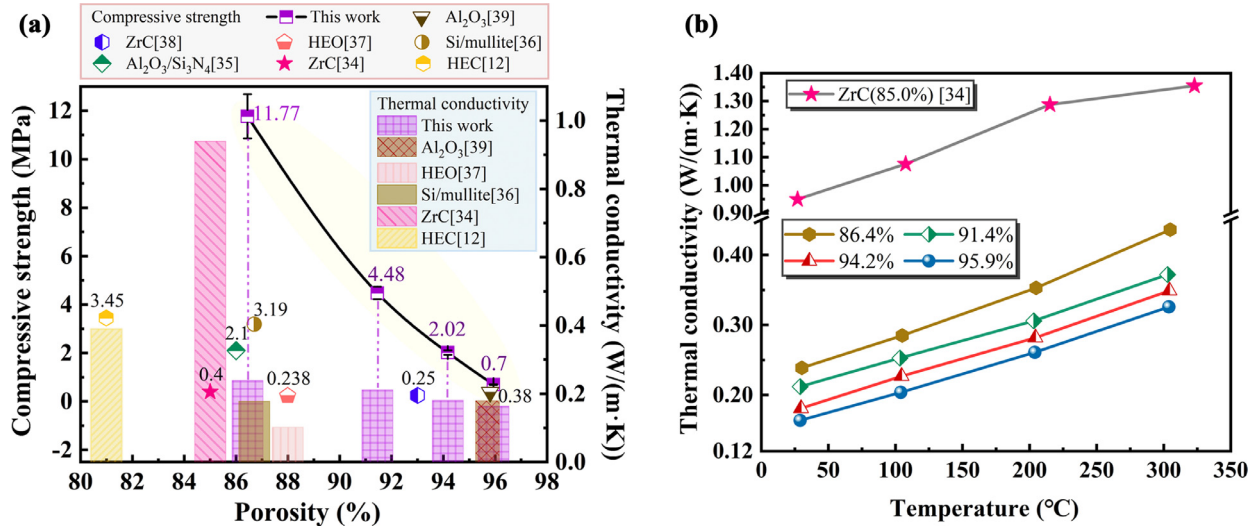

Fig. 6. (a) Compressive strength and thermal conductivity of samples with different porosities at room temperature; (b) thermal conductivity of samples with different porosities as a function of temperature.

In general, thermal conductivity of high-porosity materials at room temperature is mostly determined by heat conduction through solid skeleton. As volume fraction of solid skeleton decreases with increased porosity, room-temperature thermal conductivity gets weaker. Actually, when compared to other porous oxide ceramics with similar porosity, the thermal conductivity of our samples is slightly higher than those of typical porous Si/mullite (0.178 W/(m·K) for 86.7%) [36] and $(La_{0.2}Nd_{0.2}Sm_{0.2}Gd_{0.2}Yb_{0.2})_2Zr_2O_7$ (0.102 W/(m·K) for 88.0%) [37], but lower than that of porous Al_2O_3 (0.180 W/(m·K) for 95.9%) [39]. The main reason is that intrinsic thermal conductivity of high entropy UHTC (6.45 W/(m·K) [9] and 13.2 W/(m·K) [41]) is slightly higher than those of the oxides, such as ~6 W/(m·K) for mullite [42] and 2.5 W/(m·K) for $La_2Zr_2O_7$ [43], except for 33 W/(m·K) for Al_2O_3 [44]. Even though intrinsic thermal conductivity of carbide is very high, thermal insulation performance of ultra-high porosity high entropy carbide can still be comparable to that of conventional oxide insulation materials. Thermal conductivity of the present sample is lower than the same material system with porosity of 80.99% [12], which is benefited from higher porosity obtained by foam-gelcasting-freeze drying method. More importantly, it is worth noting that thermal conductivity of high entropy carbide is distinctly smaller than that (0.94 W/(m·K) for 85.0%) of single-component ZrC [34]. This is because high entropy effect can efficiently reduce thermal conductivity of solid skeleton due to significant phonon scattered at the disordered cation sublattice.

Besides, Fig. 6(b) plots the trends of thermal conductivity of porous samples with different porosities as a function of testing temperature. As can be seen, thermal conductivity of porous high entropy carbide slowly increases with elevated temperatures. Thermal conductivity of porous $(Zr_{1/5}Hf_{1/5}Nb_{1/5}Ta_{1/5}Ti_{1/5})C$ with porosity of 86.4% is 0.239 W/(m·K) and 0.436 W/(m·K) at room temperature and 300 °C, respectively. Moreover, the sample with higher porosity has lower thermal conductivity than those samples with lower porosity at both room and high temperatures. The values range from 0.436 W/(m·K) to 0.326 W/(m·K) when porosities increase from 86.4% to 95.9% at 300 °C. Specially, thermal conductivity for porous ZrC [34] with porosity of 85% is shown in Fig. 6(b) for comparison. From room temperature to 300 °C, thermal conductivity of ZrC has a larger variation from 0.94 W/(m·K) to 1.35 W/(m·K), which is much higher than those of porous high entropy carbide with porosity of 86.4% (from 0.239 W/(m·K) to 0.436 W/(m·K)). High entropy effect effectively reduces thermal conductivity of UHTC sample. Based on the above comparison, it is clear that our sample has enhanced mechanical and thermal properties than those carbides in previous works, as well as superior properties compared with typical oxides. Hence, it can be concluded that the specimens in this work have better comprehensive performance.

3.5. Characteristics of grain boundary

In general, intergranular amorphous films were frequently observed at grain boundary of UHTCs sintered with SiC additive in previous literatures [26,27,45]. For example, during the sintering of ZrB_2 ceramic, SiC reacted with ZrO_2 at the outset, and then ZrC and amorphous SiO_2 were formed [27]. Thus, the amorphous SiO_2 caused amorphous intergranular phase in the processed sample. Moreover, even without any additives, there was also a thin layer (~1.5 nm) of amorphous intergranular phase for high entropy (Hf-Ta-Zr-Nb)C [46], which was caused by the impurities from raw materials and ball milling process. However, the amorphous intergranular phase is a fatal weakness to high-temperature strength [28]. In this work, we used SiC as sintering additive to fabricate porous high entropy carbide $(Zr_{1/5}Hf_{1/5}Nb_{1/5}Ta_{1/5}Ti_{1/5})C$. Whereas the morphology of grain boundary is unclear in the specimen, because there exist adequate free surfaces in porous sample compared with the dense ceramic. Backscattered electron (BSE) imaging and HAADF imaging techniques were employed to further investigate the effect of SiC additive on grain boundary. It is obviously shown that there exists a striking contrast between high entropy carbide and SiC in Fig. 7(a), which is only distinguishable at high magnification. The light contrast portion is high entropy carbide $(Zr_{1/5}Hf_{1/5}Nb_{1/5}Ta_{1/5}Ti_{1/5})C$ and the relatively dark region is proven to be SiC by EDS mappings. Although SiC exists between high entropy carbide grains from BSE image, it is still worth making certain whether SiC exists in the interior of grain boundary or not on the material with porous structure.

To clarify these issues, the cross-section containing grain boundary of HEC-10 was fabricated by using a very finely focused ion beam (FIB), and microstructure of the cross-section was determined by means of scanning transmission electron microscopy (STEM). An approximately 4 μm-long grain boundary is observed in Fig. 7(b), and it is interesting to note that high entropy carbide grains are tightly bound together. There is no secondary phase or amorphous film at the interface, which is utterly different from the

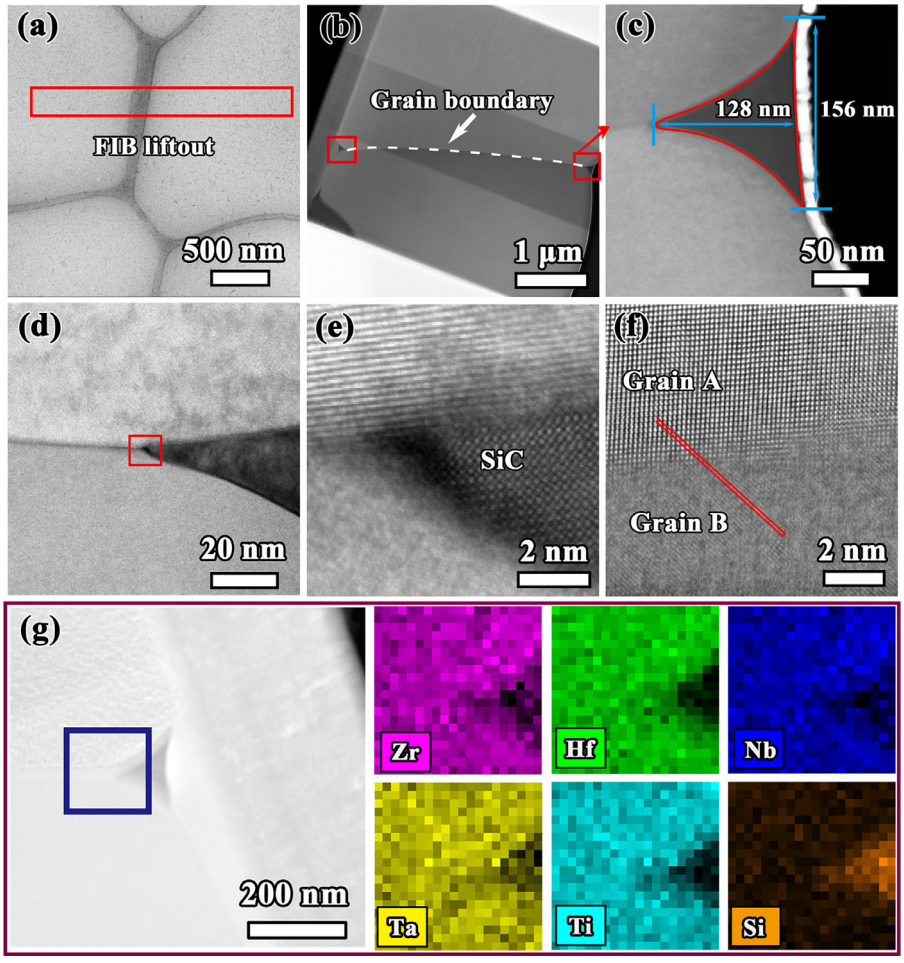

Fig. 7. (a) BSE image of cell wall surface of HEC-10, (b)-(f) HAADF images of cross-section containing grain boundary, (g) STEM and corresponding EDS mappings of porous high entropy carbide near surface of sintering neck.

morphology in previous works by using SiC additive. In contrast, the proportion of SiC is so tiny that it is easy to be neglected at low magnification. In detail, from locally enlarged HAADF image in Fig. 7(c), the presence region of SiC is like a triangle, about 156 nm in length and 128 nm in height. The final proportion of SiC estimated by HAADF image is much less than 1%, which is consistent with XRD result that there are no identified SiC diffraction peaks, because the very tiny amount of residual SiC falls below XRD detection limit. Meanwhile, SiC has a strong bonding with adjacent high entropy carbide particles as illustrated in Fig. 7(d) and (e). High-resolution transmission electronic microscopy (HRTEM) morphology displays a clean and ordered interface, and the atoms of two grains are aligned coherently as shown by the red line in Fig. 7(f). Surprisingly, SiC only locates at the pit of the surface of sintering neck between carbide grains and there is no trace of SiC in the interior of grain boundary or grains, which is confirmed again by EDS mappings in Fig. 7(g). It forecasts the good mechanical property by suppressing grain boundary softening at high temperature.

There is one inescapable fact that a small part of the interface is not particularly legible at the grain boundary as shown in HRTEM image. This is originated from huge misorientation between the two grains. It is hard to display clear atoms of two grains simultaneously. In order to further verify coherence and integrity of the interface, EDS mappings, fast Fourier transform (FFT) and inverse Fourier transform of HRTEM image at the grain boundary were used for analysis, which are supplied in Fig. 8. EDS mappings of Fig. 8(a) show that the five metal elements, Zr, Hf, Nb, Ta and Ti, also have uniform and continuous distribution even at the interface. It is confirmed that the grain boundary is clean without any segregation of elements and there is no trace of amorphous phase or SiC in the interior of grain boundary or grains. Fig. 8(b) shows HRTEM image of porous high entropy carbide sample at grain boundary. Electron diffraction patterns obtained by Fourier transform of Fig. 8(b) exhibit two sets of patterns in Fig. 8(c), namely [001] zone axis and [11$\bar{2}$] zone axis electron diffraction patterns for grains A and B, respectively. Then we select a pair of diffraction spots (200) as shown in the insert picture of Fig. 8(d) to operate inverse Fourier transform, and get neat and coherent lattice fringes. These lattice stripes extend smoothly from grain A, through the grain boundary, to grain B, which further verifies the well-ordered interface and clean grain boundary without amorphous phase.

As is well-known, most of the impurity phases in UHTCs would locate at grain boundaries [47], and even become amorphous intergranular phase. But in this study, there is no intergranular film at the grain boundaries, and SiC only exists in the pit of the surface of sintering neck between neighboring carbide grains. The reason for such result is the special porous microstructure and sintering mechanisms of porous UHTCs ceramic with SiC additive. The two conjectures are as follows. One aspect is the little addition amount (2 wt.%) of SiC, which is obviously less than that of 10 vol.%–37 vol.% of others works [22-28,47-49]. In light of sintering mechanism in literatures, TiO_2 reacts with SiC at 1550 °C

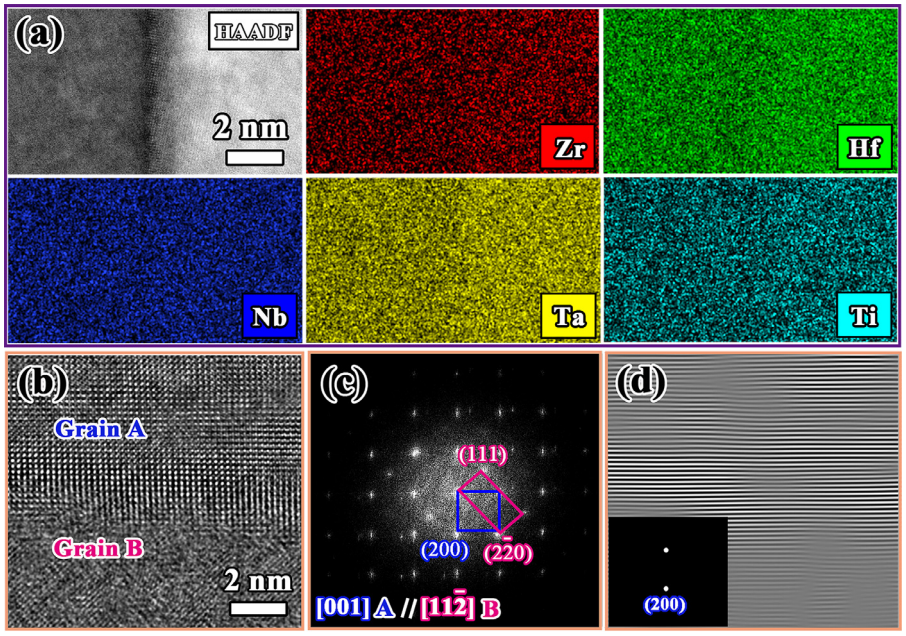

Fig. 8. (a) STEM and corresponding EDS mappings of HEC-10 at interface of matrix grains; (b) HRTEM of porous sample at grain boundary and (c) corresponding FFT image of grain A/grain B interface, (d) inverse FFT image of a selected pair of diffraction spots, while the insert shows selected pair of diffraction spots of grain A.

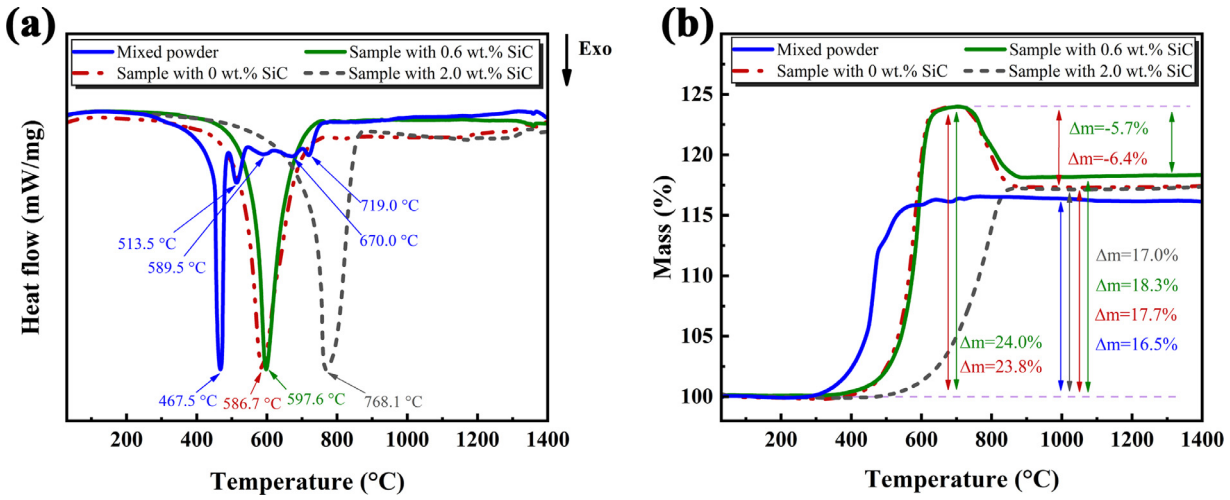

Fig. 9. (a) DSC curves of mixed powders and high entropy carbide powders with 0 wt.%, 0.6 wt.% and 2 wt.% SiC; (b) corresponding TG curves of mixed powders and high entropy carbide powders with SiC additive.

[48] and ZrO_2 reacts with SiC at 1750 °C under Ar atmosphere [49] to form liquid SiO_2 as well as gaseous SiO. In our work, during heating process, a part of SiC reacts directly with oxides on the surface of carbide particles to form gaseous SiO. Meanwhile, the transient liquid phase might appear but immediately reacts with SiC to form gaseous SiO, and most gaseous products are rapidly taken away by the flowing argon, resulting in evident consumption of SiC. Thus, there is no amorphous phase left at the grain boundary of porous sample, which accounts for the clean grain boundary in this study.

Another aspect is highly porous structure of the samples, including high porosity and thin cell wall, which bring large surface area of skeleton and unobstructed pore channel. Therefore, under incorporating SiC additive into the quinary carbides system, the contact area between carbide particles enlarges steadily with the sintering process, meanwhile the sintering neck is further strengthened. Hence, remained SiC additive is extruded to periphery of the sintering neck and finally locates at the pit of the external surface. Ultimately, a dense grain boundary is formed at the sintering neck, as shown in Fig. 2. This process is completely different from the sintering of bulk UHTCs, in which the SiC additive and carbide particles are firmly restricted inside the dense block. As temperature rises, the additive becomes liquid phase and fills in the gap of carbide particles. However, there is no free channel connected to surface of the block and thus it cannot be removed from the bulk sample. It can only appear as a second phase or bring about a thin oxide layer at the grain boundary between UHTC particles. Therefore, the very small amount of SiC additive and the unique porous structure with thin cell wall result in the clean grain boundary in the present material.

3.6. Oxidation behavior

Thermogravimetric analysis combined with differential scanning calorimetry was employed to measure the oxidation behaviors qualitatively. Fig. 9 demonstrates TG-DSC curves of the mixed raw powders and high entropy carbide powders with 0 wt.%, 0.6 wt.% and 2 wt.% SiC in air to compare oxidation behaviors. There is obvious difference between DSC curves of mixed raw powders and high entropy carbide powders in Fig. 9(a), i.e. five exothermic peaks in mixed raw powders and only one exothermic peak in high entropy carbide powders. DSC results show that the mixed raw powders and high entropy carbide powders with 0 wt.%, 0.6 wt.% and 2 wt.% SiC start to oxidize at about 274.5, 371.2, 408.7 and 523.5 °C, respectively. The mixed raw powders reach their maximum exothermic peak at ~467.5 °C, while high entropy carbide powders with 0 wt.%, 0.6 wt.% and 2 wt.% SiC are at around 586.7, 597.6 and 768.1 °C, respectively. Additionally, as shown in Fig. 9(b), TG results show that all samples exhibit weight gains, and corresponding maximum weight gain points act the same rule as maximum exothermic peak of DSC results.

The five exothermic peaks of mixed raw powders clearly correspond to sequential oxidations of the five carbide components. The single exothermic peak of high entropy carbide powders means that it really is the oxidation of a single-phase high entropy carbide. The initial oxidation temperatures and maximum exothermic peaks of high entropy carbide powders are higher than those of the mixed powders and further enhanced with more SiC addition. It shows that high entropy carbide powders have better oxidation resistance than mixed raw powders, which enhances about 119.2 °C. The addition of SiC additive also improves oxidation resistance of high entropy carbide powders, and the increment reaches 181.4 °C when the amount of SiC additive is 2 wt.%. TG-DSC results suggest that synergetic effects of high entropy modification and SiC additive effectively boost the oxidation resistance of UHTCs.

4. Conclusions

A single-phase $(Zr_{1/5}Hf_{1/5}Nb_{1/5}Ta_{1/5}Ti_{1/5})C$ with ultra-high porosity (95.9%) was successfully fabricated by foam-gelcasting-freeze drying and in-situ pressureless reaction sintering with SiC additive. To our knowledge, it ranks the highest porosity for porous ultra-high temperature ceramics reported in literatures. Porous high entropy carbide is the pure-phase with a rock-salt structure and the component is homogenous at multiple scales. Porous samples exhibit a microstructure of numerous, uniform interlinking pores and thin cell wall. The as-fabricated samples possess excellent overall performance, such as controllable ultra-high porosity (86.4–95.9%), high compressive strength (11.77–0.70 MPa) and low thermal conductivity (0.164–0.239 W/(m·K)). Due to the addition of SiC sintering additive, the sinterability of quinary ultra-high temperature carbide is obviously improved. Surprisingly, the added SiC only locates at the pit of the external surface of sintering neck between carbide grains. Most importantly, there is no secondary phase or intergranular film at the grain boundary of the thin skeleton. TG-DSC analyses indicate that high entropy carbide powders have improved oxidation resistances than mixed raw powders of five carbides and the addition of SiC additive obviously further enhances the oxidation resistances of porous high entropy UHTCs. Our work demonstrates an efficient approach to fabricate a single-phase ultra-high porosity $(Zr_{1/5}Hf_{1/5}Nb_{1/5}Ta_{1/5}Ti_{1/5})C$ with high strength, low thermal conductivity and good oxidation resistance. The as-prepared porous $(Zr_{1/5}Hf_{1/5}Nb_{1/5}Ta_{1/5}Ti_{1/5})C$ can be used in the key field of ultra-high temperature thermal insulation applications.

Declaration of Competing Interest

The authors declare that they have no known competing financial interests or personal relationships that could have appeared to influence the work reported in this paper.

Acknowledgements

We acknowledge financial support from the National Key R&D Program of China (No. 2017YFB0703201) and LiaoNing Revitalization Talents Program (No. XLYC2002018). The authors thank Dr. Ming Lv for doing some helpful TEM measurements.

References

[1] E. Wuchina, E. Opila, M. Opeka, W.G. Fahrenholtz, I.G. Talmy, Electrochem. Soc. Interface 19 (2007) 30–36.
[2] X.D. Wu, G.F. Shao, S.J. Liu, X.D. Shen, S. Cui, X.B. Chen, Powder Technol. 312 (2017) 1–10.
[3] J.N. Li, Z.J. Hu, X.T. Wang, J.X. Yang, C.C. Sun, Ceram. Int. 43 (2017) 8343–8347.
[4] J.J. Sun, Z.J. Hu, J.N. Li, H.B. Zhang, C.C. Sun, Ceram. Int. 40 (2014) 11787–11793.
[5] X.D. Wu, G.F. Shao, S. Cui, L. Wang, X.D. Shen, Ceram. Int. 42 (2016) 874–882.
[6] L.E. Toth, Transition Metal Carbides and Nitrides, Academic Press, New York, 1971.
[7] J. Haglund, A.F. Guillermet, G. Grimvall, M. Korling, Phys. Rev. B 48 (1993) 11685–11691.
[8] S.T. Oyama, The Chemistry of Transition Metal Carbides and Nitrides, Springer, Dordrecht, 1996.
[9] X.L. Yan, L. Constantin, Y.F. Lu, J.F. Silvain, M. Nastas, B. Cui, J. Am. Ceram. Soc. 101 (2018) 4486–4491.
[10] L.L. Gong, Y.H. Wang, X.D. Cheng, R.F. Zhang, H.P. Zhang, Int. J. Heat Mass Transfer 67 (2013) 253–259.
[11] H.M. Xiang, Y. Xing, F.Z. Dai, H.J. Wang, L. Su, L. Miao, G.J. Zhang, Y.G. Wang, X.W. Qi, L. Yao, H.L. Wang, B. Zhao, J.Q. Li, Y.C. Zhou, J. Adv. Ceram. 10 (2021) 385–441.
[12] H. Chen, H.M. Xiang, F.Z. Dai, J.C. Liu, Y.M. Lei, J. Zhang, Y.C. Zhou, J. Mater. Sci. 35 (2019) 1700–1705.
[13] L. Silvestroni, D. Sciti, Adv. Mater. Sci. Eng. 2010 (2010) 1–11.
[14] E. Khaleghi, Y.S. Lin, M.A. Meyers, E.A. Olevsky, Scr. Mater. 63 (2010) 577–580.
[15] L. Feng, W.G. Fahrenholtz, G.E. Hilmas, Y. Zhou, Scr. Mater. 162 (2019) 90–93.
[16] T.J. Harrington, J. Gild, P. Sarker, C. Toher, C.M. Rost, O.F. Dippo, C. McElfresh, K. Kaufmann, E. Marin, L. Borowski, P.E. Hopkins, J. Luo, S. Curtarolo, D.W. Brenner, K.S. Vecchio, Acta Mater. 166 (2019) 271–280.
[17] P. Sarker, T. Harrington, C. Toher, C. Oses, M. Samiee, J.-P. Maria, D.W. Brenner, K.S. Vecchio, S. Curtarolo, Nat. Commun. 9 (2018) 4980.
[18] X.F. Wei, J.X. Liu, F. Li, Y. Qin, Y.C. Liang, G.J. Zhang, J. Eur. Ceram. Soc. 39 (2019) 2989–2994.
[19] S.A. Ghaffari, M.A. Faghihi Sani, F. Golestani Fard, H. Mandal, J. Eur. Ceram. Soc. 33 (2013) 1479–1484.
[20] B. Shipra, K. Rishabh, B. Kantesh, Mater. Sci. Eng. A 796 (2020) 140022.
[21] R.A. Morris, B. Wang, D. Butts, G.B. Thompson, Int. J. Appl. Ceram. Technol. 10 (2013) 540–551.
[22] H.Z. Zhang, F. Akhtar, Ceramics 3 (2020) 359–371.
[23] H.Z. Zhang, F. Akhtar, Entropy 21 (2019) 474.
[24] K. Lu, J.X. Liu, X.F. Wei, W.C. Bao, Y. Wu, F. Li, F.F. Xu, G.J. Zhang, J. Eur. Ceram. Soc. 40 (2020) 1839–1847.
[25] H.X. Wang, Y.J. Cao, W. Liu, Y.G. Wang, Ceram. Int. 46 (2020) 11160–11168.
[26] S.S. Hwang, A.L. Vasiliev, N.P. Padture, Mater. Sci. Eng. A 464 (2007) 216–224.
[27] D.D. Jayaseelan, Y. Wang, G.E. Hilmas, W. Fahrenholtz, P. Brown, W.E. Lee, Adv. Appl. Ceram. 110 (2011) 1–7.
[28] D.L. Hu, H. Gu, J. Zou, Q. Zheng, G.J. Zhang, J. Materiomics 7 (2021) 69–79.
[29] Z. Wu, L.C. Sun, J.J. Pan, J.Y. Wang, J. Am. Ceram. Soc. 101 (2018) 1042–1047.
[30] J.Y. Zhou, J.Y. Zhang, F. Zhang, B. Niu, L.W. Lei, W.M. Wang, Ceram. Int. 44 (2018) 22014–22018.
[31] M. Gendre, A. Maitre, G. Trolliard, J. Eur. Ceram. Soc. 31 (2011) 2377–2385.
[32] H.L. Liu, Z.Y. Man, J.X. Liu, X.G. Wang, G.J. Zhang, J. Alloy. Compd. 729 (2017) 492–497.
[33] Z. Wu, W.P. Hu, Y.X. Luo, L.C. Sun, J.Y. Wang, J. Eur. Ceram. Soc. 38 (2018) 3347–3353.
[34] F. Li, K. Zhuang, X. Huang, X.G. Wang, G.J. Zhang, J. Eur. Ceram. Soc. 34 (2014) 3513–3520.
[35] B. Ren, Y.L. Wang, J.J. Liu, X.Y. Zhang, Y.G. Chen, Y.D. Rong, J.L. Yang, Ceram. Int. 45 (2019) 6581–6584.
[36] L.J. Zhou, Z.H. Li, Y.M. Zhu, Mater. Lett. 239 (2019) 67–70.
[37] X.Y. Meng, J. Xu, J.T. Zhu, P. Zhang, A. Rydosz, M.J. Reece, F. Gao, Scr. Mater. 194 (2021) 113714.
[38] F. Li, M.S. Liang, X.F. Ma, X. Huang, G.J. Zhang, J. Porous Mater. 22 (2015) 493–500.
[39] T. Shimizu, K. Matsuura, H. Furue, K. Matsuzak, J. Eur. Ceram. Soc. 33 (2013) 3429–3435.
[40] Z. Wu, X.P. Liang, Z.J. Shao, H.K. Chen, J.N. Li, J.Y. Wang, Materialia 18 (2021) 101158.

[41] M.D. Qin, J. Gild, C. Hu, H.R. Wang, M.S.B. Hoque, J.L. Braun, T.J. Harrington, P.E. Hopkins, K.S. Vecchio, J. Luo, J. Eur. Ceram. Soc. 40 (2020) 5037–5050.
[42] H. Schneider, J. Schreuer, B. Hildmann, J. Eur. Ceram. Soc. 28 (2008) 329–344.
[43] C.L. Wan, W. Pan, Q. Xu, Y.X. Qin, J.D. Wang, Z.X. Qu, M.H. Fang, Phys. Rev. B 74 (2006) 1–9.
[44] R.R. Monchamp, J. Solid State Chem. 12 (1975) 201–206.
[45] D. Sciti, S. Guicciardi, L. Silvestroni, Scr. Mater. 64 (2011) 769–772.
[46] J. Dusza, P. Švec, V. Girman, R. Sedlák, E.G. Castle, T. Csanádi, A. Kovalčíková, M.J. Reece, J. Eur. Ceram. Soc. 38 (2018) 4303–4307.
[47] Y. Yuan, J.X. Liu, G.J. Zhang, Ceram. Int. 42 (2016) 7861–7867.
[48] Z. Ahmadi, B. Nayebi, M.S. Asl, I. Farahbakhsh, Z. Balak, Ceram. Int. 44 (2018) 11431–11437.
[49] P. Zhang, P. Hu, X.H. Zhang, J.C. Han, S.H. Meng, J. Alloy. Compd. 472 (2009) 358–362.